Article

Employing an Artificial Neural Network in Correlating a Hydrogen-Selective Catalytic Reduction Performance with Crystallite Sizes of a Biomass-Derived Bimetallic Catalyst

Ibrahim Yakub [1,2,*], Ahmad Beng Hong Kueh [3,4,*], Edwin Andres Pineda De La O [2], Md. Rezaur Rahman [1], Mohamad Hardyman Barawi [5], Mohammad Omar Abdullah [1], Mugahed Amran [6,7,*], Roman Fediuk [8,9] and Nikolai Ivanovich Vatin [9]

1 Department of Chemical Engineering and Energy Sustainability, Faculty of Engineering, Universiti Malaysia Sarawak, Kota Samarahan 94300, Sarawak, Malaysia; rmrezaur@unimas.my (M.R.R.); amomar@unimas.my (M.O.A.)
2 Department of Chemical and Biological Engineering, University of Sheffield, Sheffield S1 4NL, UK; ep.de.la.o@msn.com
3 Department of Civil Engineering, Faculty of Engineering, Universiti Malaysia Sarawak, Kota Samarahan 94300, Sarawak, Malaysia
4 UNIMAS Water Centre (UWC), Faculty of Engineering, Universiti Malaysia Sarawak, Kota Samarahan 94300, Sarawak, Malaysia
5 Faculty of Cognitive Science and Human Development, Universiti Malaysia Sarawak, Kota Samarahan 94300, Sarawak, Malaysia; bmhardyman@unimas.my
6 Department of Civil Engineering, College of Engineering, Prince Sattam Bin Abdulaziz University, Alkharj 16273, Saudi Arabia
7 Department of Civil Engineering, Faculty of Engineering and IT, Amran University, Amran 9677, Yemen
8 Polytechnic Institute, Far Eastern Federal University, 690922 Vladivostok, Russia; fedyuk.rs@dvfu.ru
9 Peter the Great St. Petersburg Polytechnic University, 195251 St. Petersburg, Russia; vatin@mail.ru
* Correspondence: yibrahim@unimas.my (I.Y.); kbhahmad@unimas.my (A.B.H.K.); m.amran@psau.edu.sa (M.A.)

Abstract: A predictive model correlating the properties of a catalyst with its performance would be beneficial for the development, from biomass waste, of new, carbon-supported and Earth-abundant metal oxide catalysts. In this work, the effects of copper and iron oxide crystallite size on the performance of the catalysts in reducing nitrogen oxides, in terms of nitrogen oxide conversion and nitrogen selectivity, are investigated. The catalysts are prepared via the incipient wetness method over activated carbon, derived from palm kernel shells. The surface morphology and particle size distribution are examined via field emission scanning electron microscopy, while crystallite size is determined using the wide-angle X-ray scattering and small-angle X-ray scattering methods. It is revealed that the copper-to-iron ratio affects the crystal phases and size distribution over the carbon support. Catalytic performance is then tested using a packed-bed reactor to investigate the nitrogen oxide conversion and nitrogen selectivity. Departing from chemical characterization, two predictive equations are developed via an artificial neural network technique—one for the prediction of NO_x conversion and another for N_2 selectivity. The model is highly applicable for 250–300 °C operating temperatures, while more data are required for a lower temperature range.

Keywords: catalyst; selective catalytic reduction; carbon; crystallite size; artificial neural network

1. Introduction

The removal of nitrogen oxides (NO_x) from domestic and industrial emissions is of ongoing interest due to environmental benefits and the more stringent policies undertaken by many countries [1]. Many techniques have been used and studied, but the selective catalytic reduction is the most prominent. The choice of a reductant, whether ammonia, hydrocarbon, or hydrogen, is highly dependent on the available technology and

resources [2,3]. The type of reductant could influence the catalyst requirement, including the type of catalyst support, precursor, composition, operating temperature, and reactor configuration [4]. One of the most important physical properties of the selective catalytic reduction (SCR) catalyst is the microstructure of the chemical composition involved in the reaction, i.e., the microstructure of the impregnated metals. Chen et al. [5] investigated the effects of crystallite size on NO_x storage performance and concluded that the smallest size, i.e., 0.4 μm, offered the highest NO_x storage capacity while Costa et al. [6] found that the metal phase crystallinity and size played major roles in determining NO_x selectivity.

In recent years, research interest has converged on the development and employment of machine learning modeling approaches, the artificial neural network (ANN) being one of the widely adopted, due to their usefulness in forecasting numerous outcomes in the presence of multi-factorial inputs. In essence, ANN has been formulated to follow an architectural framework that mimics the thinking characteristics of the human brain. It challenges numerous input variables while making and influencing linkages amongst them to carry out prediction through three chief events, namely, training, validation, and testing. Such a predictive process follows a similar decision-formation course used by the brain when presented with a group of data. ANN gathers information from the provided input with matching outputs to form experiences and obtain knowledge through the learning of examples. With sufficient information, ANN is capable of making a reasonable forecast when presented with a new set of data. Hence, with more input data, better predicting performance is expected from ANN. Some practical uses of ANN in the literature include the prediction of concrete strength [7–9], steel connection rigidity [10], chloride permeability behaviors [11], flood identification [12], the control of vehicles [13], and medical diagnosis [14], in addition to finance [15], and countless other fields.

In this work, the hydrogen-selective catalytic reduction (H_2-SCR) was studied due to the increasing attention on the use of hydrogen as a future fuel, which could serve as the reductant in the NO_x-removal system. Considering environmental concerns, the catalyst was prepared from biomass waste, i.e., palm kernel shells (PKAC) and a mixture of two metal oxides of abundant elements, i.e., copper and iron. This bimetal oxide catalytic system could be utilized at a large scale due to its cost-effectiveness. It could be a solution to the problem of increasing biomass waste generation revolving around developing countries, in which agriculture is the primary economic activity [16]. Therefore, the possibility of applying this system using H_2-SCR to reduce NO_x from a synthetic exhaust gas is explored. This paper discusses in detail the effects of copper and iron oxide particle size on the performance of the catalysts in reducing NO_x and the development of a predictive model that correlates the particle size with the H_2-SCR performance of the catalysts.

2. Results and Discussion

2.1. FESEM-EDX

Figure 1 shows the evolution of the shape and texture of particles over the surface of the activated carbon (PKAC) and catalysts (PKAC/Cu and PKAC/Fe).

The original surface structure of PKAC was composed of coagulants of edgy particles that made up the porosity of the carbon surface. This image is similar to the SEM image obtained by Buhani et al. [17] on the activated carbon derived from palm kernel shells. As copper oxide was doped via incipient wetness, these aggregates can be seen to be reduced in size while increasing the number of particles over the surface. This is due to the thermal reaction of the carbon aggregates and additional metallic particles impregnated (refer to Figure 2) during the catalyst preparation process [18]. Similar phenomena can be observed for PKAC/Fe; however, the PKAC/Fe aggregates consist of larger particles compared to PKAC/Cu. The method used to prepare the catalysts did not change the skewness of the particle distribution.
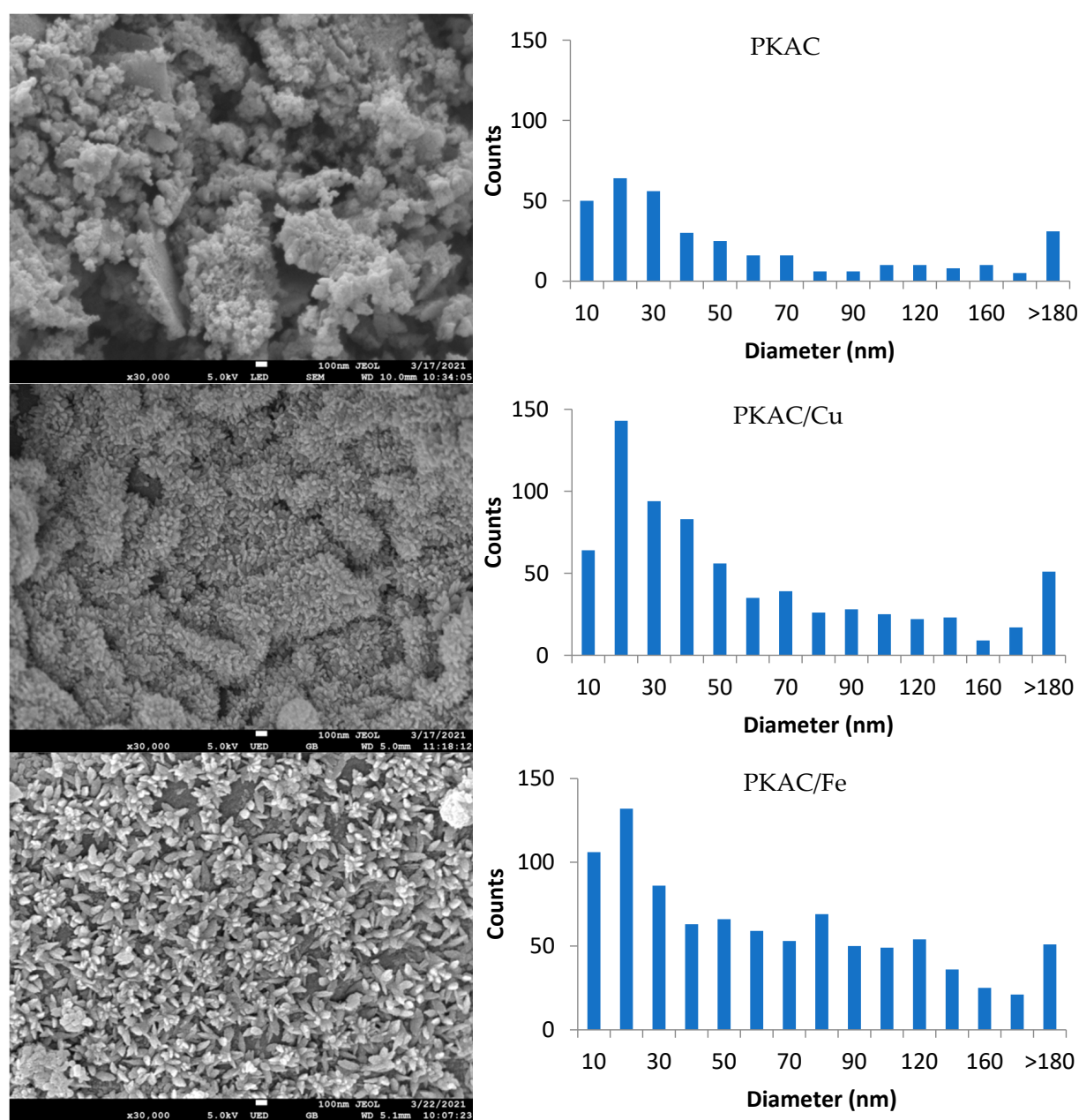
Figure 1. FESEM image and particle size distribution for PKAC and the monometallic catalysts at 30k magnification.
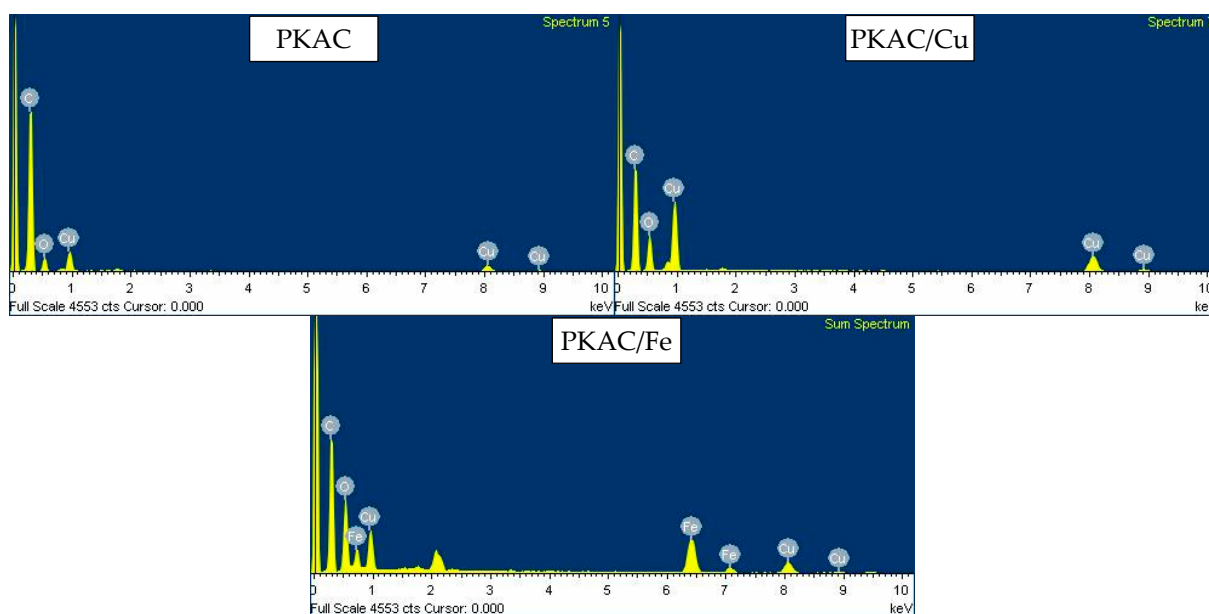
Figure 2. EDX spectra for PKAC and the monometallic catalysts at 100 magnification.

Figure 3 compares the effects of higher catalyst loading on the catalyst surface morphology. PKAC/Cu20 and PKAC/Cu30 represent catalysts with 20 wt% and 30 wt% loadings, correspondingly, as compared to only 10 wt% loading on PKAC/Cu (in Figure 1). The particle size distribution exhibits the 20 wt% loading generated particles of a more uniform size than 30 wt% loading because higher levels of particle introduction onto the surface increased the agglomeration effect (shown in orange circles). It was expected that higher agglomeration would contribute to the inactivation of the catalytic sites [19].
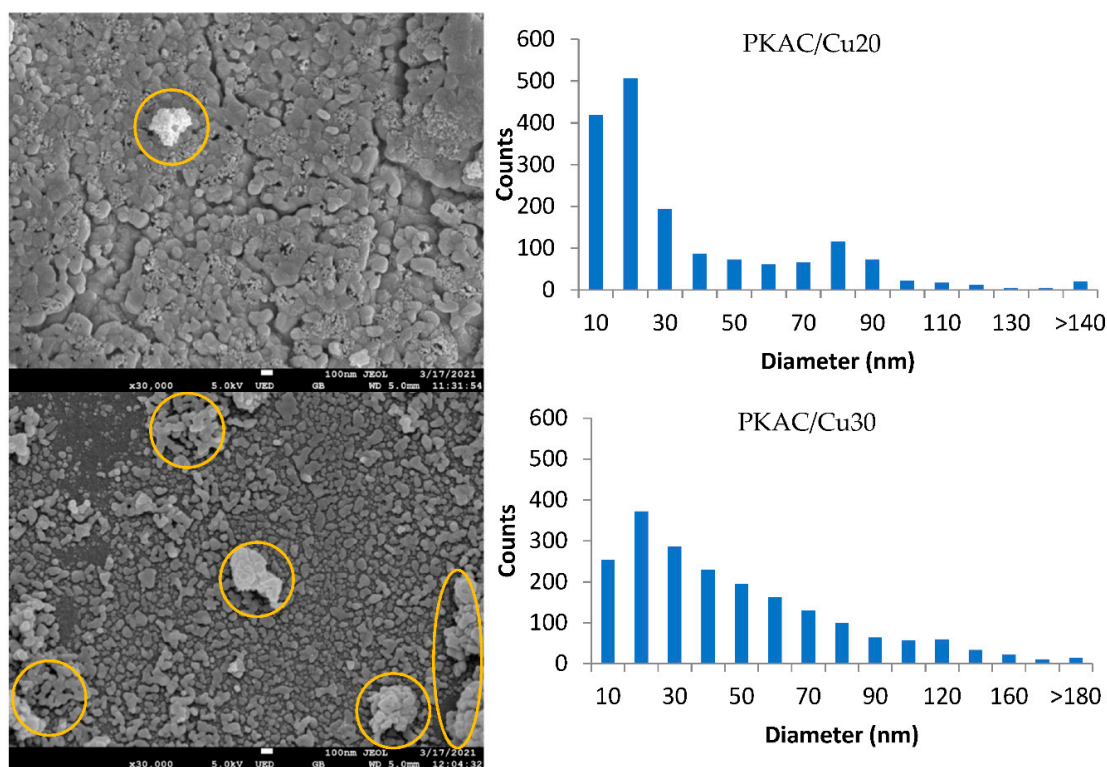
Figure 3. FESEM image and particle size distribution for higher loading monometallic catalysts at 30k magnification.

The same effect was exhibited over the bimetallic catalyst PKAC/FeCu, as shown in Figure 4. However, the agglomerates have smaller sizes compared to those observed over PKAC/Cu30 and the sizes are more uniform, as can be seen from the size distribution analysis.
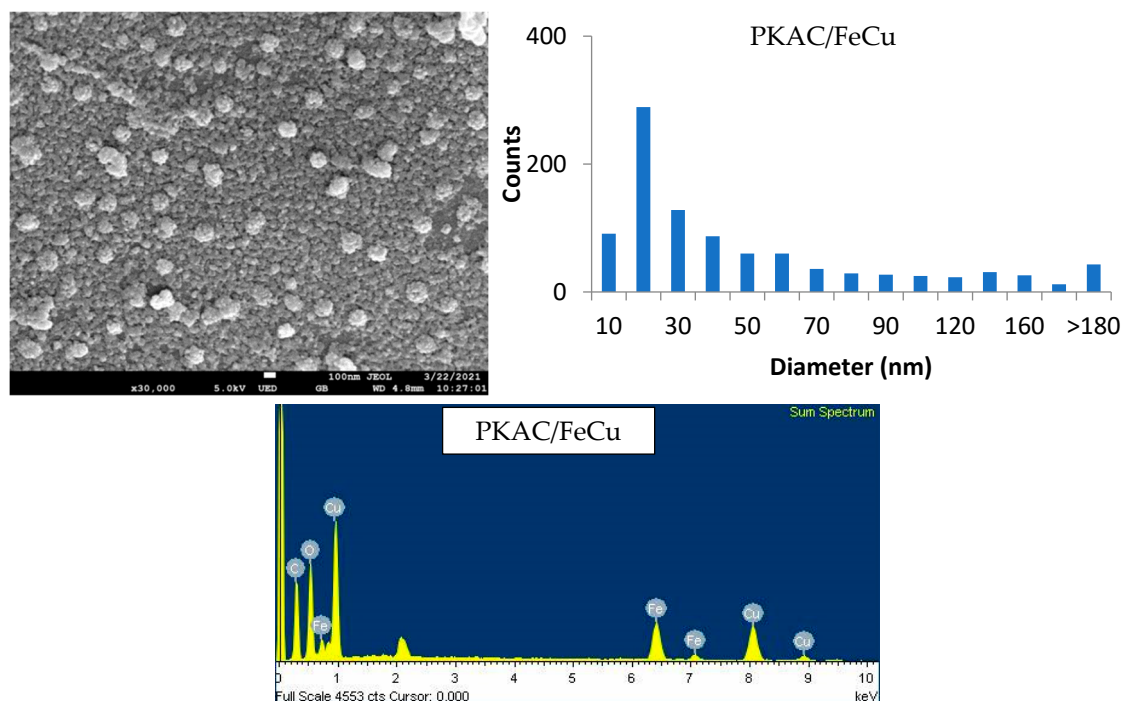
Figure 4. FESEM image, particle size distribution, and EDX spectrum for the bimetallic catalyst.

2.2. SAXS

Figure 5 shows the SAXS profiles and size distribution of the monometallic and bimetallic catalysts. The SAXS profiles were fitted to a power law described by Equation (1).

$$I(q) = q^{-\alpha} \tag{1}$$

where α is the power exponent; this calculates a simple power law with a flat background.
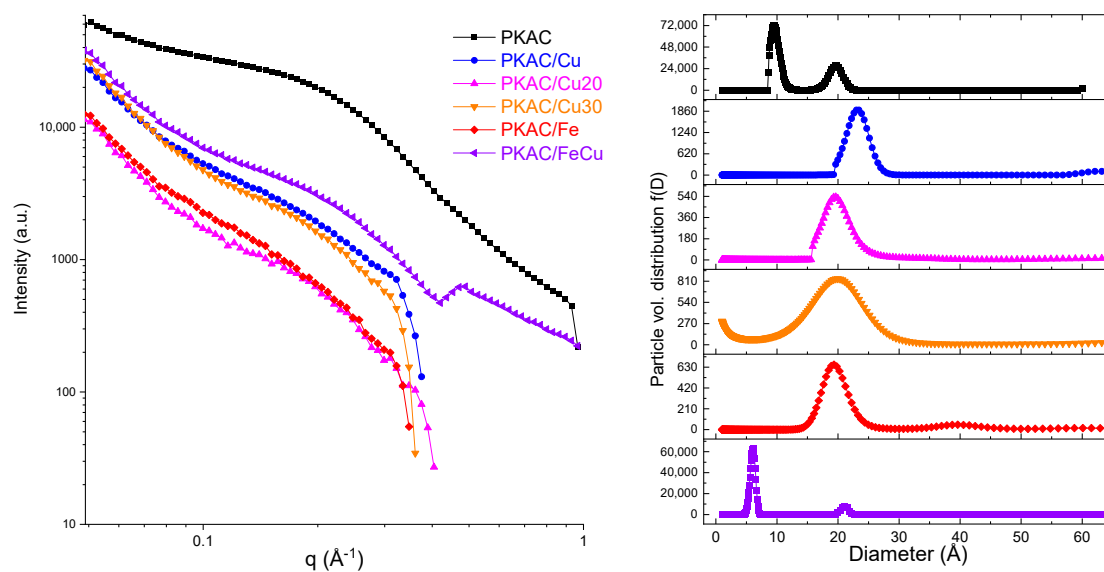
Figure 5. SAXS profiles and size distribution of monometallic and bimetallic catalysts.

The SAXS profiles show the behavior of the power law scattering with the characteristic mass fractal ($1 \leq \alpha \leq 3$). Furthermore, the power-law exponent is associated with the fractal dimension, $Ds = 6 - \alpha$; its increase indicates that the surface roughness becomes larger. The pristine PKAC presents $\alpha = 2.31 \pm 0.016$ ($Ds = 3.682$) but when the monometallic catalyst was incorporated, $\alpha = 1.85 \pm 0.021$, and $\alpha = 1.88 \pm 0.016$ for the Fe and Cu inclusions, respectively, thus demonstrating increasing trends in surface roughness. On the other hand, increasing the amount of the monometallic catalyst (copper loading) increased α from 1.88 ± 0.016 to 2.24 ± 0.01, while smoothing the surface morphology. A more complicated behavior of the power law exponent was observed when bimetallic catalysts were used: for the samples with 20 wt% of Cu and with 10 wt% each of Fe and Cu, α changed from 2.31 ± 0.16 to 2.11 ± 0.25 and 1.62 ± 0.006, respectively.

Subsequently, the size distribution of monometallic and bimetallic catalysts was developed using Igor Pro. The particle size distribution analysis of the PKAC sample shows two different sizes, 9.47 Å and 19.26 Å, the former being the dominant size of the sample. When monometallic catalysts were used, most of them showed a bigger size than the pristine PKAC. The main size in PKAC (9.47 Å) could have worked as a seed or nucleation center, and, therefore, bigger sizes are observed in the samples with additives. Increasing the amount of Cu on the pristine PKAC, the size distribution analysis shows a shift to smaller sizes, from 23.27 Å to around 20 Å, on the samples containing 20 wt% and 30 wt% of Cu. A similar trend was observed when the bimetallic catalyst was used, with a larger size than the pristine PKAC, in the order of 20 Å. However, when Cu and Fe were used together, a smaller size (6.13 Å) was dominant, which is likely due to the presence of unreacted raw material.

2.3. WAXS

More information could be obtained by knowing which particle belongs to which active sites. This may be achieved through the WAXS analysis that can reveal the species and crystal structure information of the catalysts. Figure 6 displays the WAXS patterns obtained for all catalysts in this study.
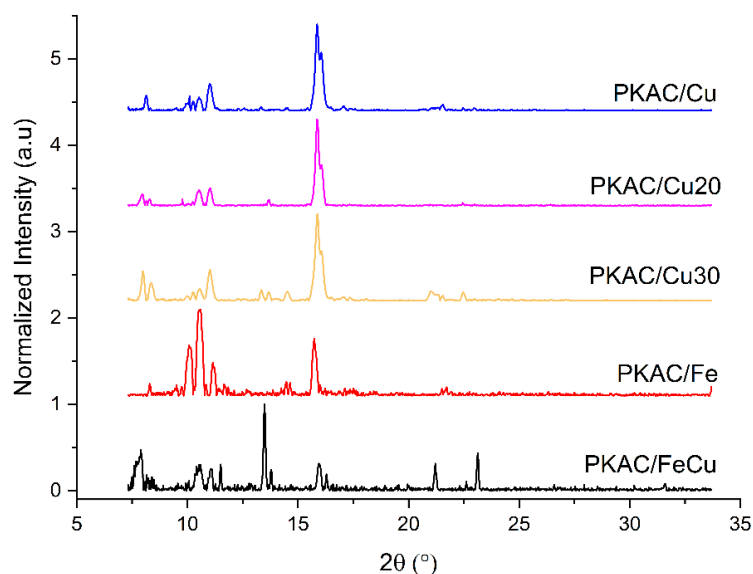
Figure 6. WAXS patterns for monometallic and bimetallic catalysts.

The copper species detected on PKAC/Cu, PKAC/Cu20, and PKAC/Cu30 include Cu (at 16°), CuO (at 13, 14, 22, and 23°), and Cu_2O (at 15.5°) [20], with the latter exhibiting the highest crystallinity. The increment of copper loading saw an increase in intensity, especially for Cu_2O. Meanwhile, the iron species observable in PKAC/Fe included only Fe_2O_3 (at 12, 14.5, and 16°) [21] with very low intensity, thereby showing the almost

amorphous behavior of the catalyst and indicating the species was highly dispersed into the surface pores. Furthermore, a dramatic decrease in intensity was seen for the copper species when the catalyst was co-impregnated with iron, which also decreased crystallite sizes. There are certainly synergistic effects when combining the two catalysts over biomass-activated carbon, as the crystallization and dispersion effects are altered by increasing the monometallic loading [22].

Synergism between copper and iron in NO_x reduction was reported by Ma et al. [23], who concluded that the bimetallic catalysts increased NO oxidation to NO_2 as well as the adsorption of NO_2 and NH_3, which accelerated the reaction. However, dependence on the performance of this bimetallic catalyst (Fe-Cu) supported over activated carbon in H_2-SCR on the composition of the two metals, to our knowledge, has not been reported in the literature. Therefore, the present work intends to reveal the effects of a different combinations of Fe-Cu impregnation loadings on the performance of the catalyst. The catalysts were prepared with each metal loading in the range of 10 wt% to 30 wt% and were analyzed for the metal content via AAS (refer Section 3.5). The resulted metal composition is summarized in Table S1 (Supplementary Material). The ratio between Fe and Cu loadings is plotted against the most dominant size of the catalyst (obtained from WAXS studies), as shown in Figure 7.
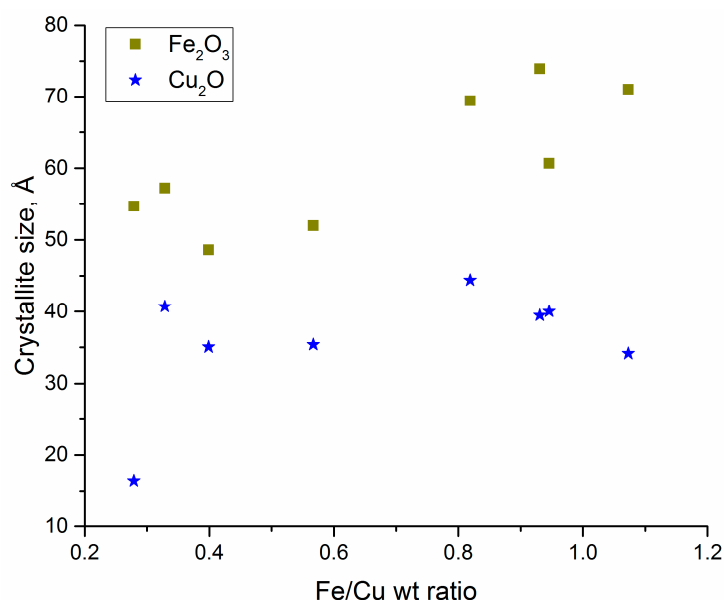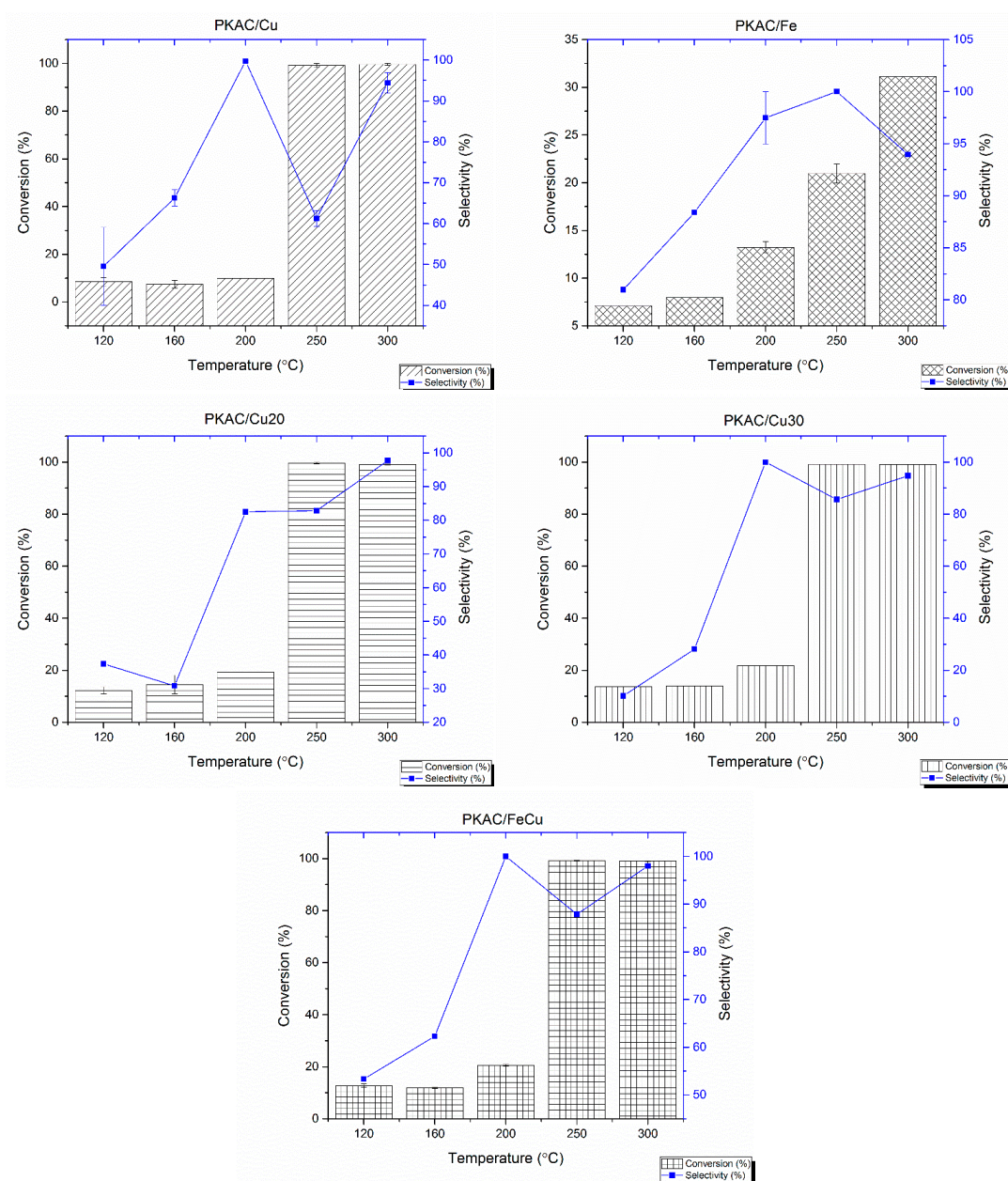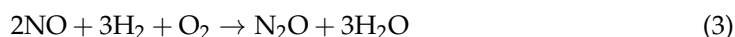

Figure 7. Effects of the pairing metals ratio on crystallite size.

The plot shows that over all ranges of metal ratios under study, co-impregnation between iron and copper via subsequent incipient wetness produced particles of nano-size, and the doping of different amounts of copper over iron influenced the crystallite size of both metals. With smaller amounts of copper doped over the iron-impregnated carbon, from a ratio of 0.2 to 0.8, Fe_2O_3 particles increased in size while Cu_2O kept an almost constant crystallite size. Thereafter, Fe_2O_3 exhibits an increase in size while the size of Cu_2O crystals decreases. Nevertheless, Fe_2O_3 always has a larger crystallite size compared to Cu_2O over the studied ranges of metal ratios. It is interesting to conclude from the plot that the crystal growth over activated carbon is controlled by the relative concentration of the metals during incipient wetness.

2.4. Catalyst Activity

Figure 8 shows the performance of the synthesized catalysts in terms of NO_x conversion and N_2 selectivity at different temperatures. Due to the toxicity of NO_x gas used in the experiment, only selected runs were repeated to obtain the standard deviation. The error bars can be seen to be only significant at lower temperatures when PKAC/Cu was used,

but when iron was co-impregnated (PKAC/FeCu), the error bars became insignificant over all temperatures. Furthermore, both NO_x conversion and N_2 selectivity were low at lower temperatures for all catalysts, while the catalyst activity improved at elevated temperatures (higher than 200 °C). The selectivity was highest at 200 °C for all catalysts even though the NO_x removal was still below 25%, while the conversion was highest at 300 °C for all catalysts. It was determined in this study that the selectivity is low due to the formation of by-products, especially nitrous oxide (N_2O) and ammonia (NH_3), indicating that the following reactions ((2) to (4)) occurred simultaneously (where M is metal catalyst site) [6];

$$2NO + 4H_2 + O_2 \rightarrow N_2 + 4H_2O \tag{2}$$

$$2NO + 3H_2 + O_2 \rightarrow N_2O + 3H_2O \tag{3}$$

$$M - N + 3M - H \rightarrow 4M + NH_3 \tag{4}$$
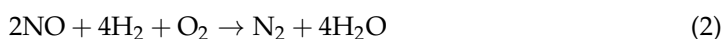
Figure 8. Catalytic activity (NO_x conversion and N_2 selectivity) for the monometallic and bimetallic oxide catalysts.

It can be noticed that the range of selectivity achieved by the bimetallic catalyst (PKAC/FeCu) improved in comparison to the monometallic catalyst of the same catalyst dosage (PKAC/Cu20), increasing from 30–98% to 50–100%. As discussed in the succeeding sections, this was contributed to by the different crystallite sizes where higher catalyst dosage exhibited agglomeration, while the incorporation of a second metal reduced the agglomerate size.

Therefore, it is important to investigate the influence of different crystallite sizes on the performance of bimetallic catalysts in the NOx reduction system. By varying the Fe/Cu ratio and determining the catalyst activity, the following sections extend the use of this information to predict the performance of a newly developed iron-copper catalyst by analyzing the crystallite size.

2.5. Prediction of NO_x Removal

Figure 9 displays the performance curve produced by the ANN model, which indicates that the best validation performance was achieved at epoch 1, for a total of 7 epochs. The training status in predicting NO_x conversion percentage, X, is observed in Figure 10. It is noticed that the validation stops after 7 epochs, replicating the same viewpoint as that exhibited in Figure 9. It is demonstrated in Figure 10c that after epoch 1, the error occurs 6 times, implying incidents of data-overfitting. Therefore, the weighted values computed at epoch 1 are employed to construct the desired descriptive model from the ANN training.
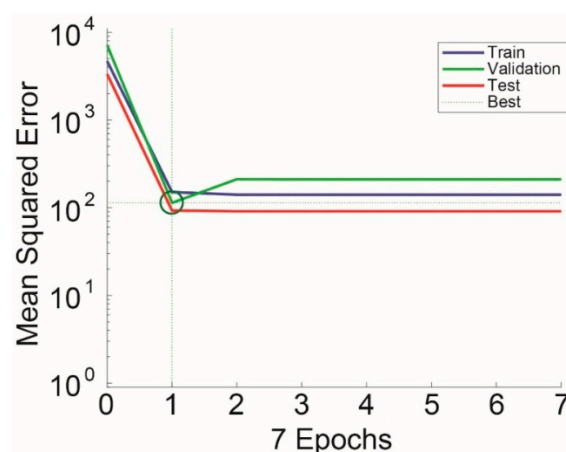

**Figure 9.** Performance curve for predicting NO_x conversion percentage, X.

The ANN-regressed outcomes are inspected in Figure 11 in terms of training, validation, test, and overall responses. In these subfigures, 'Target' values indicate the 'measured X', while the 'Output' values are the predicted X, as calculated by the ANN model. A set of somewhat high R^2 values are produced in each of these steps. Even so, due to the lack of data, the data points are concentrated near the early and end regions of all regressed curves. The computed relationship for predicting X, as determined in the form of Equation (12), takes the following form:

$$X = [0.519412 \quad 0.072857 \quad 0.057157]P_i - 52.2415 \tag{5}$$

Equation (5) demonstrates the best forecasting ability in determining X for both temperatures of 250 °C and 300 °C, displaying errors ranging merely from 4.4 to 9.4%. Under the influence of lower temperatures, the errors of prediction could go as high as 76%. This is attributed to two reasons. Firstly, the input data fed to the ANN model are insufficient to offer enough examples for ANN learning. Secondly, selective catalytic reduction favors a higher range of temperatures. Temperatures in the higher regime seem to be the optimal condition for the conversion of NO_x. This observation is later replicated in Section 2.6 in terms of N_2 selectivity.
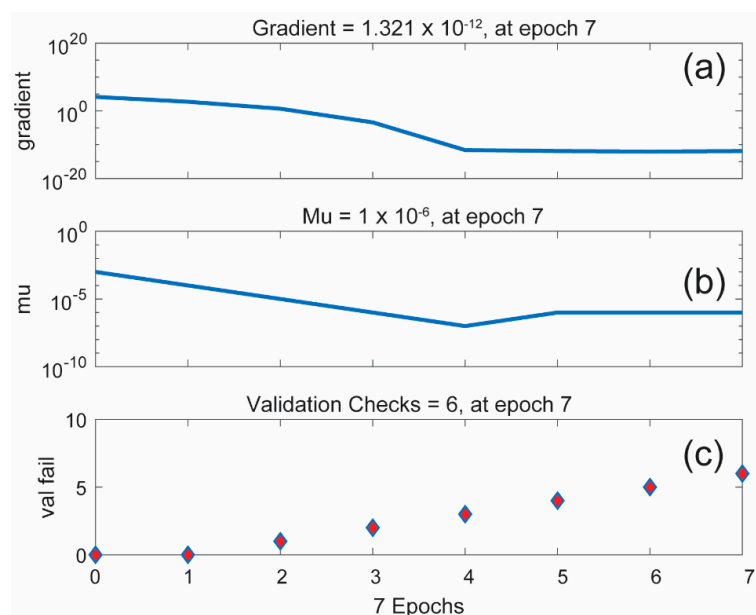
Figure 10. Training status in predicting the NO$_x$ conversion percentage, *X*: (**a**) Gradient (**b**) momentum term (**c**) validation checks.
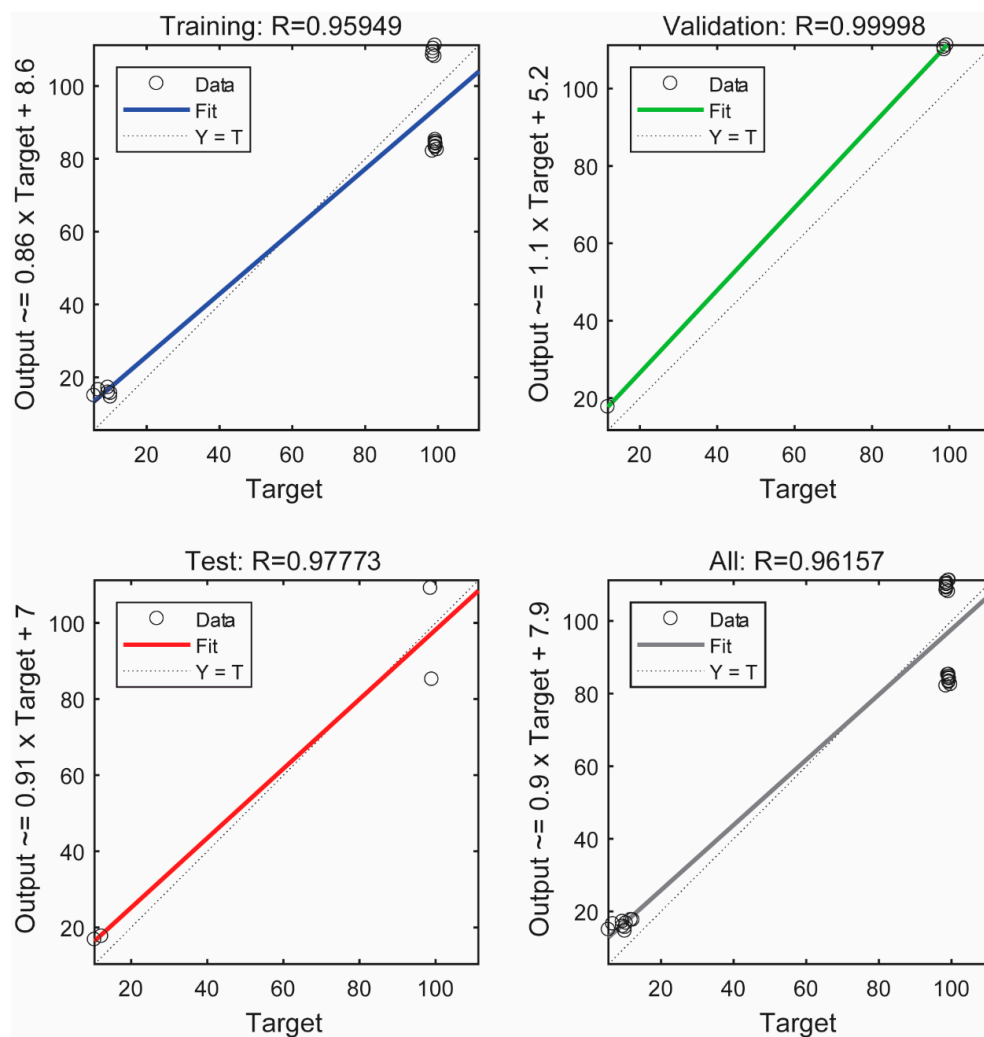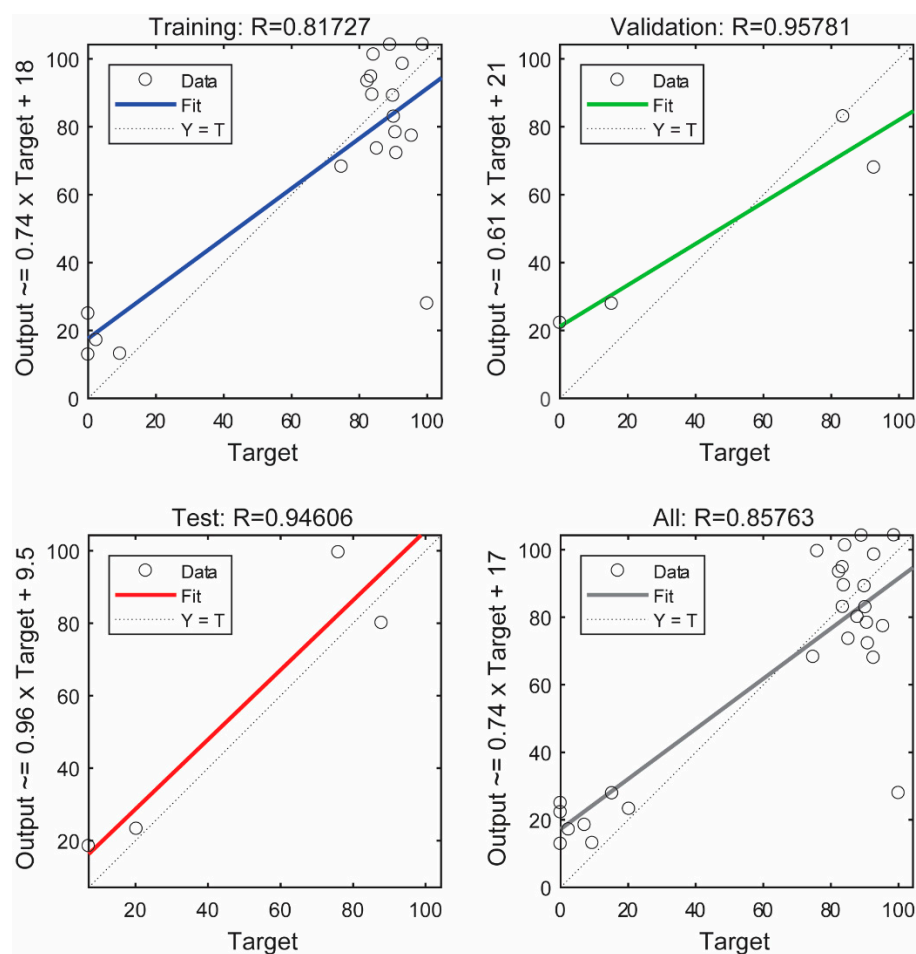

Figure 11. Training, validation, test, and overall regressed outcomes for predicting *NO*$_x$ conversion.

2.6. Prediction of N_2 Selectivity

The regression plots in the case of N_2 selectivity are shown in Figure 12. Again, data points are populated near both edges in all subfigures. In comparison to Figure 11, the R^2 coefficients are slightly lower. This is due to a slightly more dispersed arrangement of data points, relative to those presented in Figure 11. Having specified this, it should be emphasized that using the same amount of data for training in predicting the NO_x conversion has resulted in a high R-value in Figure 11. The explicit mathematical expressions derived from the ANN model for predicting N_2 selectivity are obtained as shown in Equation (6):

$$S = [0.423943 \quad 0.36269 \quad 0.347461]P_i - 63.518 \tag{6}$$

Figure 12. Training, validation, test, and overall regressed outcomes for predicting N_2 selectivity.

The strong predictive ability, noted in Section 2.5, for NO_x conversion is also replicated here for the high-temperature range between 250 °C and 300 °C. Errors found in conforming to measure outcomes range from 0.3 to 15.3%, the range of which is slightly wider compared to the prediction of the NO_x conversion. In the presence of lower temperatures, the errors increase to 3.7–100%. Upon closer inspection, 100% errors are found in the cases of 0 N_2 selectivity, suggesting a numerical issue rather than the modeling capability of the proposed ANN model.

Nevertheless, it is worth noting, given the two main reasons described, that the prediction of the measured outcomes (target) by the explicit analytical model derived from the ANN, remains within a well-acceptable regime of accuracy. In general, Equations (5) and (6) effectively capture the determination of the percentages of NO_x conversion and N_2 selectivity, respectively, specifically in the presence of the high temperatures of 250 °C and 300 °C. The model capability could surely be improved through the provision of a larger dataset.

This could also imply that at low temperatures, the chemical processes were not well-optimized or did not fully interact, thereby causing low predictability of the formulated models. A future study is recommended to resolve this observation.

3. Materials and Methods

3.1. Materials

Palm kernel shell-activated carbon (PKAC) was obtained from a local supplier in Sarawak, Malaysia. The metal salts used in this study were copper (II) nitrate trihydrate ($Cu(NO_3)_2.3H_2O$, 99.999%) and iron (III) nitrate nonahydrate ($Fe(NO_3)_3.9H_2O$, 99.999%). All were supplied by Sigma Aldrich, Gilligham, UK.

3.2. Catalyst Preparation

No further pre-treatment was required for PKAC besides drying in an oven (Memmert GmbH + Co. KG, Schwabach, Germany) at 110 °C for 72 h to remove the adsorbed water and carbon dioxide. The carbon was ground using a ball mill and sieved to particle sizes of 600 μm–710 μm [24,25]. Metallic catalysts were doped over the carbon via the incipient wetness method with a 1:1 ratio of activated carbon pore volume to metal salt solution volume. Consequentially, the wastewater produced via this method was largely reduced. The catalyst was then washed and filtered using deionized water and dried at 80 °C for 24 h before calcination at 350 °C and 510 °C for Cu and Fe, respectively (based on the decomposition temperature of the metal nitrates), under a helium ambient (to prevent excessive carbon combustion, which could lower the carbon mass). Two types of catalyst designs were investigated: monometallic and bimetallic catalysts. The former involved impregnating the metals individually over carbon, while the latter was synthesized by combining two metals using sequential impregnation. The catalyst loading was 10 wt% unless otherwise specified to be 20 and 30 wt%, which were denoted as PKAC/MX (M = metal, X = 20 or 30) for monometallic oxide catalysts, and as $PKAC/M_1X_1M_2X_2$ for bimetallic oxide catalysts (M_1 = first metal, X_1 = loading of first metal, M_2 = second metal, and X_2 = loading of second metal).

3.3. Field Emission Scanning Electron Microscopy and Energy Dispersive X-ray

Surface morphology and the dispersion of metallic catalysts were studied using a NOVA NANOSEM 230 Ultra High-Resolution Scanning Electron Microscope (FEI, Hillsboro, OR, USA) at an accelerating voltage of 5 kV and working distance between 4.5 and 10.0 mm. At a magnification of 30,000 times, the particles in the samples were analyzed using Image-J software to determine their size distribution following the protocol published by [26]. The error from using this method was reported to be less than 2% [27]. The equipped Energy Dispersive X-ray Spectroscopy (EDX) was employed to inspect the distribution of the active sites over the carbon surface.

3.4. Small-Angle and Wide-Angle X-ray Scattering

Measuring the atomic spatial arrangement on a scale down to 10^{-8} cm is usually achieved by the application of diffraction. A diffraction pattern, obtained upon the recording of scattering waves over a material, was found to correlate with the crystal structure of a particular material. Three types of suitable waves for this process are X-ray, electron, and neutron [28]. Small-angle X-ray scattering (SAXS) is a powerful technique used to investigate material structures at large distances. It helps to determine the shape, size distribution, and surface structure of particles much smaller than those observed by optical microscopy or by the naked eye. Typically, sizes ranging from 1μm to several Å are measured. While wide-angle X-ray scattering (WAXS) has been used to determine lattice constants of some particles similar to X-ray diffraction (XRD), it is typically carried out along with SAXS. The size of the nano-crystal is determined using the Scherrer formula with the breadth values of the WAXS diffraction peaks.

In this project, SAXS and WAXS were employed to evaluate the crystalline phase and size of the catalysts impregnated over the carbon support. This was performed at a 9ID beamline at the Advanced Photon Source, Argonne National Laboratory, Lemont, IL, USA. For this, powdered samples were prepared and placed on the sample seats. The facility used synchrotron light produced from the acceleration of electrons as the source of the high-energy and high-brightness X-ray beams, with a monochromatic beam of the generated X-ray (21 keV) bombarded over the sample. This caused the atomic electrons to move and generated a scattering wave. A detector placed behind the specimen collected the scattered wave and recorded the intensity of the wave at a range of incidence angles, θ. This generated a diffraction pattern in a 2D image that was converted into 1D data for analysis [29]. In this study, the data collection time was about 2 min. In addition, profiles of blank air were subtracted as background and instrumental slit smearing was removed during data reduction. For visualization, intensity data were placed on an absolute intensity scale. Bragg's law relates the incident wavelength, λ, to the interplanar spacing, *d*, between atoms in the specimen, as presented in Equation (7). Each interplanar spacing is a plane of dimension labeled by Miller indices (*hkl*). A peak at this location implies the existence of this plane, which is also measured as 2θ, as expressed in Equation (8):

$$2d\sin\theta = \lambda \tag{7}$$

$$2\theta = 2arcsin\left(\frac{\lambda\sqrt{h^2 + k^2 + l^2}}{2a_0}\right) \tag{8}$$

The diffraction pattern of a specimen was then matched with the Joint Committee on Powder Diffraction Standards (JCPDS), which maintains a large collection of diffraction patterns for thousands of materials. A computer program, such as Igor Pro 8 [29], was used for peak matching, peak search, and fitting for the crystallite size calculation. The latter was calculated using the Scherer Equation (9):

$$L = \frac{K\lambda}{B(2\theta)cos\theta} \tag{9}$$

where *L* is the mean size of crystallite diameter, *K* is the shape factor depending on the crystallite shape (with a value of 0.9 often near many shape factors), and $B(2\theta)$ is the full width at half the maximum intensity of the peak (FWHM).

3.5. Metal Content Determination

The composition of metals in the carbon-based catalysts was measured by digesting the catalyst in an acidic solution for chemical element analysis in atomic absorption spectroscopy (AAS). In AAS, samples containing metals were atomized in an air-acetylene flame to produce an analyte of the excited state, which absorbed a specific wavelength unique to a particular element. The source of the wavelength emission was a hollow-cathode lamp made of cobalt-chromium-copper-iron-manganese-nickel (depending on the element of interest), and the intensity of absorbance related to the concentration of the analyte via the Beer-Lambert law [30]. Approximately 5 mL of sample was injected into the Analyst 400 AA (PerkinElmer, Inc., Massachusetts, UK), which automatically calculated the concentration of the metal based on the calibration carried out prior to the sample run. Subsequently, the Fe/Cu ratio was calculated based on the mass of each metal in the catalyst.

3.6. Catalyst Activity

The catalysts were tested for the nitric oxide reduction capacity in terms of NO conversion and N_2 selectivity. Approximately 1 g of the catalyst was placed inside a fixed-bed reactor before being reduced in-situ at 250 °C under 5% H_2/He at 7175 h^{-1}. Subsequently, the system was cooled/heated to the desired temperature, in the range of 120 to 300 °C before feeding in a gas mixture of 500 ppm NO + 4% H_2 + 1.5% O_2 in

helium. The gas exiting the system was analyzed continuously using an HPR-20 mass spectrometer (Hiden, Warrington, UK). NO conversion and N_2 selectivity were calculated via Equations (10) and (11):

$$\text{Conversion, } X\ (\%) = \frac{F_{NOx,in} - F_{NOx,out}}{F_{NOx,in}} \times 100\% \tag{10}$$

$$\text{Selectivity, } S_{N_2}(\%) = \frac{2 \times F_{N_2}}{\sum aF_p} \times 100\% \tag{11}$$

where $F_{NOx,in}$, $F_{NOx,out}$, F_{N2}, F_p, and a are the flow rates of NO_x at the inlet and outlet, flow rate of nitrogen at the outlet, flow rate of each product, and the number of nitrogen moles in each of the products' molecules, respectively.

3.7. Artificial Neural Network Model

To begin the modeling, the input data were first subcategorized into three subsets according to the following settings: training (70%), validation (15%), and test (15%). In brief, the training step exercises allows the subset to learn from examples, such that an acceptable accuracy is reached for a certain number of epochs; the validation step displays how well this subset has been trained in estimating the modeled behaviors; and the test step demonstrates the performance of the trained subset. In the current scope, only three inputs were considered: temperature (x_1), iron crystallite size (x_2), and copper crystallite size (x_3) with two separate outputs, i.e., the NO_x conversion percentage (%) and N_2 selectivity percentage (%). Therefore, for the training of the ANN model, the factors or independent variables that influence the performance of the nitric oxide reduction (Section 3.6) are temperature, iron crystallite size, and copper crystallite size. These three parameters were defined as the inputs. To measure the performance of the nitric oxide reduction, the NO_x conversion percentage and N_2 selectivity percentage, as determined in Section 3.6, for various sets of temperature, iron crystallite size, and copper crystallite size, were taken as the outcomes (dependent variables) or the parameters to be predicted by the to-be-formulated ANN equations. The MATLAB ANN program was employed with the network architecture as presented in Figure 13. The computation was compartmentalized into four components, i.e., input, hidden layers, an output layer, and output. The feed-forward backpropagation algorithm was selected as the network type. It was proven by Khademi et al. [8] that one hidden layer is enough to provide good predictability for a multi-layer network, the choice of which is evidenced also in numerous existing works. Thus, only one hidden layer was employed in the present study with one output layer. Further, the Levenberg-Marquardt algorithm was adopted as the training function with the mean squared normalized error as the chosen performance function. The pure linear transfer function, *PURELIN*, was utilized for both the hidden and output layers. Furthermore, seven hidden neuron nodes were used in the hidden layer following the ($2n + 1$) function, where n = number of input variables.
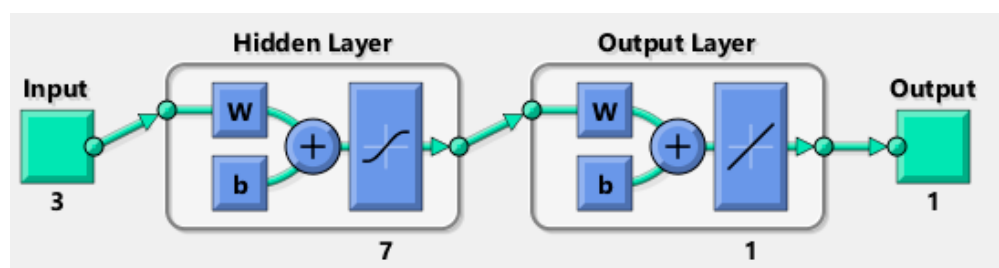

Figure 13. ANN architecture adopted in MATLAB.

ANN-Derived Symbolical Model

The desired responses, in the current-case NO_x conversion percentage, *X* (%), and N_2 selectivity percentage, *S* (%), were computed in the vectorized output form. It is noteworthy that a separate ANN model was formulated for *X* and *S*. Furthermore, it is notable that most existing ANNs have been used to produce the desired results in numeric form only. For practicality, it is convenient to formulate a symbolical model that can be reused for future predictions for the same input and output types without having to rerun the ANN. The formulation of such a model is described as follows:

By setting *n* = 7 neurons, the input weight matrix, *IW*, of $n \times m$ size and hidden layer bias matrix, b_1, of $n \times 1$ size are obtained, where *m* = number of input variables. Accordingly, the output layer has a layer weight matrix, $LW_{1 \times n}$, and an output layer bias matrix, $b_{2(1 \times 1)}$. The universal mathematical expression between input variables and output response is explicitly defined by Equation (12):

$$R = \xi_i P_i + \eta \tag{12}$$

where *R* and P_i are the output and input vectors, respectively, ξ_i is the weighted responsiveness ratio vector, and η is the weighted bias constant. ξ_i and η are, respectively, defined in Equations (13) and (14), while the remaining Equations (15)–(21) are related to the ANN computation.

$$\xi_i = \sum_{i=1}^{m} \frac{\hat{R}_2}{\hat{P}} w_i \tag{13}$$

$$\eta = \frac{\hat{R}_1 + \hat{R}_2 \gamma}{2} - \sum_{i=1}^{m} \left\{ \frac{\hat{R}_2}{\hat{P}} w_i P_{i\ min} + \frac{\hat{R}_2}{2} w_i \right\} \tag{14}$$

whereas,

$$\hat{R}_1 = R_{max} + R_{min}, \ \hat{R}_2 = R_{max} - R_{min}, \hat{P} = P_{i\ max} - P_{i\ min} \tag{15}$$

such that

$$a = LW\, b_1 + b_2 \tag{16}$$

with w_i described by

$$w_i = LW \times IW \tag{17}$$

The *IW*, *LW*, b_1, and b_2 matrices are generated as weighted products by the ANN model. The intermediate matrices are defined by *T*, T_1, and T_2, with the transferring function of the pure linear type, *PURELIN*.

$$T = IWP + b_1 \ \ or \ \ T_j = \sum_{j=1}^{n} \sum_{i=1}^{m} IW_{ji} P_i + b_{1j} \tag{18}$$

$$T_1 = purelin(T) = T \tag{19}$$

$$T_2 = LWT_1 + b_2 \ \ or \ \ T_2 = \sum_{j=1}^{n} LW_j T_{1j} + b_2 \tag{20}$$

$$R = purelin(T_2) = T_2 \tag{21}$$

in which *m* = 3 and *n* = 7 in the current case. By defining the input parameters, $P_i = \{x_1, x_2, x_3\}^T$, and the corresponding output, *R* as *X* and *S*, are then determined.

4. Conclusions

The effects of copper and iron oxides' crystallite sizes on their performance in reducing NO_x, and the development of a predictive model that correlates the crystallite size with H_2-SCR performance, had been discussed. Two types of catalyst designs were investigated—monometallic and bimetallic catalysts doped over palm kernel shell-activated carbon. Observation on the catalyst surface via FESEM showed that PKAC/FeCu possessed

particles of uniform size. Furthermore, SAXS analysis revealed that the particle size distribution shifted to the left (smaller sizes) when there was an increase in metal composition in monometallic catalysts. When copper and iron oxides were co-doped, the dominant particle size reduced even more, down to 6.13 Å. Using WAXS analysis, it was discovered that there were various crystal phases of metal oxides on PKAC/FeCu, with copper having the highest crystallinity. It was found that the concentration of copper metals affects the crystal phase and sizes of the bimetallic catalyst. The performance of the various combinations of Cu and Fe bimetallic catalysts in reducing NO_x was tested in a fixed-bed reactor and calculated in terms of NO_x conversion and N_2 selectivity. Two predictive equations were developed to determine the performance of the catalysts based on temperature and crystallite size, both showing high reliability at the high-temperature range of 250–300 °C. Notwithstanding, further improvements to this model could be achieved with more data from both low and high temperatures. Lower predictability could be relevant to the less optimal performance or only partial occurrence of interaction at lower temperatures. These are two open areas for exploration in future studies.

References

1. Chin, T.Y.; Yakub, I.; Hin, T.Y.Y. Evaluation of Catalysts Derived from Palm Kernel Shell Carbon in a Passive NO_x Removal from a Diesel Engine Exhaust. *Emiss. Control Sci. Technol.* **2020**, *6*, 336–344. [CrossRef]
2. Ratnasari, A.; Syafiuddin, A.; Kueh, A.B.H.; Suhartono, S.; Hadibarata, T. Opportunities and Challenges for Sustainable Bioremediation of Natural and Synthetic Estrogens as Emerging Water Contaminants Using Bacteria, Fungi, and Algae. *Water Air Soil Pollut.* **2021**, *232*, 242. [CrossRef]
3. Ratnasari, A.; Zaidi, N.S.; Syafiuddin, A.; Boopathy, R.; Kueh, A.B.H.; Amalia, R.; Prasetyo, D.D. Prospective Biodegradation of Organic and Nitrogenous Pollutants from Palm Oil Mill Effluent by Acidophilic Bacteria and Archaea. *Bioresour. Technol. Rep.* **2021**, *15*, 100809. [CrossRef]
4. Kim, H.S.; Kasipandi, S.; Kim, J.; Kang, S.H.; Kim, J.H.; Ryu, J.H.; Bae, J.W. Current Catalyst Technology of Selective Catalytic Reduction (Scr) for NO_x Removal in South Korea. *Catalysts* **2020**, *10*, 52. [CrossRef]
5. Chen, Z.; Wang, M.; Wang, J.; Wang, C.; Wang, J.; Li, W.; Shen, M. Investigation of Crystal Size Effect on the NO_x Storage Performance of Pd/SSZ-13 Passive NO_x Adsorbers. *Appl. Catal. B Environ.* **2021**, *291*, 120026. [CrossRef]
6. Costa, C. An Investigation of the $NO/H_2/O_2$ (Lean De-NO_x) Reaction on a Highly Active and Selective $Pt/La_{0.7}Sr_{0.2}Ce_{0.1}FeO_3$ Catalyst at Low Temperatures. *J. Catal.* **2002**, *209*, 456–471. [CrossRef]

7. Nikoo, M.; Torabian Moghadam, F.; Sadowski, Ł. Prediction of Concrete Compressive Strength by Evolutionary Artificial Neural Networks. *Adv. Mater. Sci. Eng.* **2015**, *2015*, 849126. [CrossRef]

8. Khademi, F.; Akbari, M.; Jamal, S.M.; Nikoo, M. Multiple Linear Regression, Artificial Neural Network, and Fuzzy Logic Prediction of 28 Days Compressive Strength of Concrete. *Front. Struct. Civ. Eng.* **2017**, *11*, 90–99. [CrossRef]

9. Tan, W.L.; Lee, Y.H.; Tan, C.S.; Lee, Y.Y.; Kueh, A.B.H. Mechanical Properties and Fracture Prediction of Concretes Containing Oil Palm Shell and Expanded Clay for Full Replacement of Conventional Aggregates. *J. Teknol.* **2022**, *84*, 171–181. [CrossRef]

10. Kueh, A.B.H. Artificial Neural Network and Regressed Beam-Column Connection Explicit Mathematical Moment-Rotation Expressions. *J. Build. Eng.* **2021**, *43*, 103195. [CrossRef]

11. Boğa, A.R.; Öztürk, M.; Topcu, I.B. Using ANN and ANFIS to Predict the Mechanical and Chloride Permeability Properties of Concrete Containing GGBFS and CNI. *Compos. Part B Eng.* **2013**, *45*, 688–696. [CrossRef]

12. Abhyankar, A.; Patwardhan, A.; Paliwal, M.; Inamdar, A. Identification of Flooded Areas Due to Severe Storm Using Envisat ASAR Data and Neural Networks. *J. Civ. Eng. Sci. Technol.* **2019**, *10*, 124–131. [CrossRef]

13. Zissis, D.; Xidias, E.K.; Lekkas, D. A Cloud Based Architecture Capable of Perceiving and Predicting Multiple Vessel Behaviour. *Appl. Soft Comput.* **2015**, *35*, 652–661. [CrossRef]

14. Alizadeh, E.; Lyons, S.M.; Castle, J.M.; Prasad, A. Measuring Systematic Changes in Invasive Cancer Cell Shape Using Zernike Moments. *Integr. Biol.* **2016**, *8*, 1183–1193. [CrossRef] [PubMed]

15. French, J. The Time Traveller's CAPM. *Invest. Anal. J.* **2017**, *46*, 81–96. [CrossRef]

16. Tan, M.; Yakub, I.; YH, T.-Y. Passive Nitrogen Oxides Removal from a Diesel-Engine Exhaust Gas Using a Biomass-Carbon Catalyst. *J. Appl. Sci. Process Eng.* **2020**, *7*, 479–488. [CrossRef]

17. Buhani, B.; Puspitarini, M.; Rahmawaty, R.; Suharso, S.; Rilyanti, M.; Sumadi, S. Adsorption of Phenol and Methylene Blue in Solution by Oil Palm Shell Activated Carbon Prepared by Chemical Activation. *Orient. J. Chem.* **2018**, *34*, 2043–2050. [CrossRef]

18. Ukanwa, K.S.; Patchigolla, K.; Sakrabani, R.; Anthony, E. Preparation and Characterisation of Activated Carbon from Palm Mixed Waste Treated with Trona Ore. *Molecules* **2020**, *25*, 5028. [CrossRef]

19. Liu, H.X.; Li, S.Q.; Wang, W.W.; Yu, W.Z.; Zhang, W.J.; Ma, C.; Jia, C.J. Partially Sintered Copper–ceria as Excellent Catalyst for the High-Temperature Reverse Water Gas Shift Reaction. *Nat. Commun.* **2022**, *13*, 867. [CrossRef]

20. Kikhtyanin, O.; Pospelova, V.; Aubrecht, J.; Lhotka, M.; Kubička, D. Effect of Atmosphere Calcination and Temperature on the Hydrogenolysis Activity and Selectivity of Copper-Zinc Catalysts. *Catalysts* **2018**, *8*, 446. [CrossRef]

21. Van Everbroeck, T.; Ciocarlan, R.G.; Van Hoey, W.; Mertens, M.; Cool, P. Copper-Containing Mixed Metal Oxides (Al, Fe, Mn) for Application in Three-Way Catalysis. *Catalysts* **2020**, *10*, 1344. [CrossRef]

22. Shen, B.; Chen, J.; Yue, S.; Li, G. A Comparative Study of Modified Cotton Biochar and Activated Carbon Based Catalysts in Low Temperature SCR. *Fuel* **2015**, *156*, 47–53. [CrossRef]

23. Ma, Z.; Yang, H.; Li, Q.; Zheng, J.; Zhang, X. Catalytic Reduction of NO by NH_3 over Fe-Cu-O_x/CNTs-TiO_2 Composites at Low Temperature. *Appl. Catal. A Gen.* **2012**, *427–428*, 43–48. [CrossRef]

24. Nikmatin, S.; Syafiuddin, A.; Kueh, A.B.H.; Purwanto, Y.A. Effects of Nanoparticle Filler on Thermo-Physical Properties of Rattan Powder-Filled Polypropylene Composites. *J. Teknol.* **2015**, *77*, 181–187. [CrossRef]

25. Drahman, S.H.; Kueh, A.B.H.; Zainal Abidin, A.R.; Nikmatin, S. Efficient Cumulative Breakage Distribution and Breakage Rate Computation with Minimal Experiment Intervention Incorporating Optimal Time Determination for Fine Grinding Simulation. *Powder Technol.* **2018**, *329*, 313–322. [CrossRef]

26. Yolanda, Y.D.; Nandiyanto, A.B.D. How to Read and Calculate Diameter Size from Electron Microscopy Images. *ASEAN J. Sci. Eng. Educ.* **2021**, *2*, 11–36. [CrossRef]

27. Andrialovanirina, N.; Ponton, D.; Behivoke, F.; Mahafina, J.; Léopold, M. A Powerful Method for Measuring Fish Size of Small-Scale Fishery Catches Using ImageJ. *Fish. Res.* **2020**, *223*, 105425. [CrossRef]

28. Fultz, B.; Howe, J. *Transmission Electron Microscopy and Diffractometry of Materials*, 2nd ed.; Springer: Berlin/Heidelberg, Germany, 2002.

29. Ilavsky, J.; Zhang, F.; Andrews, R.N.; Kuzmenko, I.; Jemian, P.R.; Levine, L.E.; Allen, A.J. Development of Combined Microstructure and Structure Characterization Facility for in Situ and Operando Studies at the Advanced Photon Source. *J. Appl. Crystallogr.* **2018**, *51*, 867–882. [CrossRef]

30. Ball, D.W. *Field Guide to Spectroscopy*; Society of Photo Optical: Bellingham, WA, USA, 2006.